



RESEARCH ARTICLE

10.1029/2023SW003436

Extreme Relativistic Electron Fluxes in GPS Orbit: Analysis of NS41 BDD-IIR Data

Nigel P. Meredith¹ , Thomas E. Cayton² , Michael D. Cayton², and Richard B. Horne¹ 

¹British Antarctic Survey, Natural Environment Research Council, Cambridge, United Kingdom, ²Santa Fe, NM, USA

Key Points:

- The 1 in 100 year flux at $L = 4.5$ ranges from $9.0 \times 10^6 \text{ cm}^{-2}\text{s}^{-1}\text{sr}^{-1} \text{ MeV}^{-1}$ at $E = 0.6 \text{ MeV}$ to $56 \text{ cm}^{-2}\text{s}^{-1}\text{sr}^{-1} \text{ MeV}^{-1}$ at $E = 8.0 \text{ MeV}$
- The 1 in 100 year flux at $L = 6.5$ ranges from $6.9 \times 10^5 \text{ cm}^{-2}\text{s}^{-1}\text{sr}^{-1} \text{ MeV}^{-1}$ at $E = 0.6 \text{ MeV}$ to $6.0 \text{ cm}^{-2}\text{s}^{-1}\text{sr}^{-1} \text{ MeV}^{-1}$ at $E = 8.0 \text{ MeV}$
- The fluxes of relativistic electrons with energies in the range $0.6 \leq E \leq 2.0 \text{ MeV}$ in the region $4.25 \leq L \leq 4.75$ have a robust upper bound

Correspondence to:

N. P. Meredith,
nmer@bas.ac.uk

Citation:

Meredith, N. P., Cayton, T. E., Cayton, M. D., & Horne, R. B. (2023). Extreme relativistic electron fluxes in GPS orbit: Analysis of NS41 BDD-IIR data. *Space Weather*, 21, e2023SW003436. <https://doi.org/10.1029/2023SW003436>

Received 17 JAN 2023

Accepted 10 APR 2023

Abstract Relativistic electrons in the Earth's outer radiation belt are a significant space weather hazard. Satellites in GPS-type orbits pass through the heart of the outer radiation belt where they may be exposed to large fluxes of relativistic electrons. In this study we conduct an extreme value analysis of the daily average relativistic electron flux in Global Positioning System orbit as a function of energy and L using data from the US NS41 satellite from 10 December 2000 to 25 July 2020. The 1 in 10 year flux at $L = 4.5$, in the heart of the outer radiation belt, decreases with increasing energy ranging from $8.2 \times 10^6 \text{ cm}^{-2}\text{s}^{-1}\text{sr}^{-1} \text{ MeV}^{-1}$ at $E = 0.6 \text{ MeV}$ to $33 \text{ cm}^{-2}\text{s}^{-1}\text{sr}^{-1} \text{ MeV}^{-1}$ at $E = 8.0 \text{ MeV}$. The 1 in 100 year is a factor of 1.1–1.7 larger than the corresponding 1 in 10 year event. The 1 in 10 year flux at $L = 6.5$, on field lines which map to the vicinity of geostationary orbit, decrease with increasing energy ranging from $6.2 \times 10^5 \text{ cm}^{-2}\text{s}^{-1}\text{sr}^{-1} \text{ MeV}^{-1}$ at $E = 0.6 \text{ MeV}$ to $0.48 \text{ cm}^{-2}\text{s}^{-1}\text{sr}^{-1} \text{ MeV}^{-1}$ at $E = 8.0 \text{ MeV}$. Here, the 1 in 100 year event is a factor of 1.1–13 times larger than the corresponding 1 in 10 year event, with the value of the factor increasing with increasing energy. Our analysis suggests that the fluxes of relativistic electrons with energies in the range $0.6 \leq E \leq 2.0 \text{ MeV}$ in the region $4.25 \leq L \leq 4.75$ have an upper bound. In contrast, further out and at higher energies the fluxes of relativistic electrons are largely unbounded.

Plain Language Summary Relativistic electrons in the Earth's outer radiation belt are a significant space weather hazard. Global Navigation Satellite Systems such as the US Global Positioning System (GPS), the European Galileo navigation system, the Russian GLONASS system, and the Chinese Beidou system operate in medium Earth orbit at altitudes between 19,000 and 24,000 km. They all pass through the heart of the outer radiation belt where they may be exposed to large fluxes of relativistic electrons. In this study we conduct an extreme value analysis of the daily average relativistic electron flux in GPS orbit as a function of position and energy using data from the US NS41 satellite from 10 December 2000 to 25 July 2020. We determine the 1 in 10, 1 in 50 and 1 in 100 year relativistic electron flux levels as a function of position and energy. The 1 in N year relativistic electron fluxes determined here serve as benchmarks against which to compare other extreme space weather events and to help assess the potential impact of an extreme space weather event.

1. Introduction

Modern society is increasingly reliant on satellites for a wide variety of applications including communication, navigation, Earth observation, and defense. For example, in 2021, the overall global space economy generated revenues of \$386 billion, an increase of 4% compared to 2020 (Satellite Industry Association, 2022). This ever growing infrastructure is increasingly vulnerable to the potentially damaging effects of space weather (Krausmann, 2011). The concern at government level in the UK is such that severe space weather was added to the UK National Risk Register of Civil Emergencies in 2011, where the likelihood of the reasonable worst case scenario occurring in the next year is currently estimated to be between 1 in 20 and 1 in 100 (HM National Risk Register, 2020).

The impacts of space weather on satellite operations range from momentary interruptions of service to total loss of capabilities when a satellite fails. For example, during a major storm in 2003, 47 satellites experienced anomalies, more than 10 satellites were out of action for more than 1 day, and the joint US-Japanese US\$640M Midori 2 environmental research satellite was a complete loss (Webb & Allen, 2004).

Relativistic electrons ($E > 0.5 \text{ MeV}$) are a major source of radiation damage to satellites. These, so-called “killer” electrons can penetrate satellite surfaces and embed themselves in insulating materials and ungrounded conductors. Here, the charge can accumulate over time resulting in the build up of high electric fields which

© 2023. The Authors.

This is an open access article under the terms of the [Creative Commons Attribution License](https://creativecommons.org/licenses/by/4.0/), which permits use, distribution and reproduction in any medium, provided the original work is properly cited.

may eventually exceed breakdown levels (Frederickson et al., 1991; Rodgers & Ryden, 2001). The subsequent discharge can cause electric circuit upsets, damage components and, in exceptional cases, prove fatal for a satellite (e.g., Koons & Fennel, 2006). Indeed, significant correlations have been found between satellite anomalies and the fluxes of $E > 2$ MeV electrons (Iucci et al., 2005; Wrenn et al., 2002).

Relativistic electrons in near Earth space are generally confined to two distinct regions referred to as the inner and outer radiation belt. The inner radiation belt typically occurs at altitudes from 650 to 6,500 km in the Earth's magnetic equatorial plane, and the outer radiation belt at altitudes from 13,000 to 40,000 km. The region in between is known as the slot region and is usually devoid of relativistic electrons. The inner belt is relatively stable with significant variations only occurring during the most intense geomagnetic storms (Baker et al., 2007). In contrast, the outer radiation belt is highly dynamic, especially during geomagnetic storms. Here the fluxes of relativistic electrons may change by orders of magnitude on timescales ranging from minutes to weeks (e.g., Baker et al., 1994; Blake et al., 1992). This variability is controlled by a variety of transport, acceleration and loss mechanisms (e.g., Li & Hudson, 2019; Shprits, Elkington, et al., 2008; Shprits, Subbotin, et al., 2008; Thorne, 2010), all of which become enhanced during enhanced geomagnetic activity. The location of the peak of the flux of relativistic electrons is also highly variable, typically lying at altitudes in the range 14,000–28,000 km (Meredith et al., 2003).

Our critical infrastructure extends to 6.6 Earth radii, encompassing a region which includes the Earth's inner radiation belt and the bulk of the outer radiation belt. As of 30 April 2022 there were 5,465 operational satellites in Earth orbit, including 4,700 in low Earth orbit (LEO), 140 in Medium Earth Orbit (MEO), 60 in elliptical orbits and 565 in geostationary orbit (GEO) (<https://www.ucsusa.org/resources/satellite-database>). Most are exposed to relativistic electrons at some or all points in their orbits. Satellites in MEO are exposed to relativistic electrons from the outer edge to the heart of the outer radiation belt while satellites in GEO are exposed to relativistic electrons toward the edge of the outer radiation belt. Satellites in LEO are exposed to relativistic electrons in the inner radiation belt and, for those in high inclination LEO orbits, also to relativistic electrons at high magnetic latitudes where they cross field lines which are connected to the outer radiation belt.

Satellite operators and engineers require realistic estimates of the highest fluxes that are likely to be encountered in a particular satellite orbit to assess the impact extreme events on the satellite fleet and to improve resilience of future satellites by better design of satellite components if required. Satellite insurers also require this information to ensure satellite operators are doing all they can to reduce risk and to help them evaluate realistic disaster scenarios. Previous studies have determined the 1 in 10 and 1 in 100 year event for relativistic electrons in GEO using data from the Energetic Particle Sensors on board the National Oceanic and Atmospheric Administration (NOAA) GOES satellites (Meredith et al., 2015) and High Earth orbit (HEO) using data from the Radiation Environment Monitor (IREM) on board European Space Agency (ESA's) INTEGRAL spacecraft (Meredith et al., 2017), for energetic electrons in LEO using data from the Medium Energy Proton and Electron Detectors on board the NOAA POES satellites (Meredith et al., 2016a) and for internal charging currents in MEO using data from the SURF instrument on board ESA's Giove-A satellite (Meredith et al., 2016b). The results from these studies have been used in the development of space weather reasonable worst case scenarios for the UK National Risk Assessment (Hapgood et al., 2021). Furthermore, the 1 in 100 year relativistic electron fluxes from GEO and HEO were included in the US Space Weather Phase 1 Benchmarks report (US Space Weather Phase 1 Benchmarks, 2018).

Global Navigation Satellite Systems (GNSSs) such as the US Global Positioning System (GPS), the European Galileo navigation system, the Russian GLONASS system, and the Chinese Beidou system operate in MEO at altitudes between 19,000 and 24,000 km. They all thus pass through the heart of the outer radiation belt where they may be exposed to large fluxes of relativistic electrons. GNSS-enabled devices are used ubiquitously all over the world for navigation, positioning, tracking, mapping and timing. For example, in 2021 there were 6.5 billion GNSS devices in use and this is expected to rise to 10.3 billion by 2031 (EUSPA EO & GNSS Market Report, 2022). In 2021 the global downstream market revenue from both GNSS-enabled devices and services was 199 billion Euros and this is expected to grow to 492 billion Euros by 2031, largely fueled by expected revenues from added value services (EUSPA EO & GNSS Market Report, 2022). It is therefore important to have a comprehensive understanding of the environment encountered by satellites in GNSS-type orbits and, in particular, knowledge of the likely extremes of this environment to be able to better protect space assets operating in this region.

In this study we use approximately 20 years of data from the US GPS NS41 satellite to determine the 1 in 10, 1 in 50, and 1 in 100 year space weather event for relativistic electrons in GPS orbit as a function of energy and L . We first sorted the data by satellite location and calculated the daily average fluxes as a function of energy, L and time. We then computed probability distributions as a function of energy and L . We then conducted extreme value analyses to determine the 1 in 10, 1 in 50, and 1 in 100 year flux as a function of energy and L . The instrumentation and data analysis are described in Section 2 and the probability distributions are presented in Section 3. The extreme value analysis technique is described in Section 4 and the results are presented in Section 5. Finally, the results are discussed and the conclusions presented in Sections 6 and 7 respectively.

2. Instrumentation and Data Analysis

2.1. Instrumentation

The data used in this study were collected by the Burst Detector Dosimeter IIR (BDD-IIR) on board the US GPS satellite NS41. NS41 was launched on 10 November 2000 and operated in a circular orbit at an altitude of 20,200 km with an inclination of 55° and a period of 12 hr. It crossed the magnetic equator around $L = 4.2$ and sampled higher L shells at higher magnetic latitudes. For this study we use data from the entire mission, extending from 10 December 2000 to 25 July 2020.

BDD-IIR is a multi purpose silicon detector system. It features 8 individual channels of a “shield/filter/sensor” design that permits the detector to sample roughly half the celestial sphere while at the same time shielding the silicon sensor elements from most of the incident particle flux. Absorbers in front of the sensors determine the energy thresholds for measuring the incident particle fluxes. The aperture dimensions were chosen in an attempt to achieve equal counting rates in all channels. During on-orbit operation none of the BDD-IIR's channels appeared to saturate. Background counting rates were found to be well behaved. For each week of data mean values of the counting rates of the 8 channels were compiled from accumulations reported from L values larger than 20. Except for weeks with one or more solar energetic particle (SEP) events, the weekly mean values were used for the background counting rates for each of the 2,520 individual records. During SEPs, the background estimation followed the evolution of the SEP and were time dependent.

The deposited energy thresholds were calibrated carefully (Cayton et al., 1998). Electron response functions for the channels were determined by detailed modeling of the instrument by Monte Carlo methods (Tuszewski et al., 2002). The version of the channel response functions used to compute the fluxes studied here were determined from Monte Carlo simulations that exposed the entire BDD-IIR instrument to isotropic fluxes of mono-energetic electrons (Cayton et al., 2010). These response functions correspond to incident electrons in the energy range 0.1–10 MeV, and involve no scaling factors.

The electron response functions are most sensitive to the highest energy incident electrons. Any electron spectrum covering the energy range from 0.1 to 10 MeV can be folded with the response functions to predict counting rates in all eight channels due to that spectrum. Adding background counting rates to these yields a set of model counting rate that may be compared directly with the measured rates (corrected for the measured 6 ms dead-time). Best-fitting relativistic-Maxwellian spectra were determined by minimizing the sum of squared differences of a set of model counting rates (background plus ones due the spectrum of electrons) and the set of dead-time corrected measured counting rates. Least-squares fitting was attempted only when three or more of the observed (and corrected) rates exceeded the mean background counting rates by more than 3 standard deviations. Each of the best-fitting spectra covers the energy range 0.1–10 MeV. Commonly observed spectral features (i.e., remarkably exponential shapes) of relativistic electrons in the outer radiation belt (Cayton et al., 1989; Pierrard & Lemaire, 1996; Reagan et al., 1981) provided guidance for the selection of the relativistic Maxwellian as the functional form for these model spectra.

For energies greater than 0.5 MeV, electron fluxes computed from this set of response functions compared very well with pitch-angle resolved ones mapped up B-field lines to NS41 from the Synchronous Orbit Particle Analyzer (SOPA, Version 3) aboard S/C LANL-97A during calendar year 2005; below 0.5 MeV the single-component spectra from BDD-IIR consistently underestimated those mapped from geostationary orbit: an additional spectral component is needed to adequately represent the energetic electron population in the energy range 0.1–0.5 MeV. The standard “space-weather data” used here model the electron spectrum as a single component; we therefore restrict attention to the relativistic electron population with energies greater than 0.5 MeV.

Single relativistic-Maxwellian fits of the BDD-IIR observations at high magnetic latitude contributed to a density and temperature description of energetic electrons in the Earth's magnetotail (Denton & Cayton, 2011). Using instrument specific response functions evaluated for incident electrons in the energy range 0.1–10 MeV, that involve no scaling factors, the procedure described above yielded consistent spectra for NS41 and 11 other GPS spacecraft during the 5-year interval January 2006 through November 2010: NS48 (BDD-IIRM), and NS53–NS62 (Combined X-ray and Dosimeter). Data from BDD-IIR have been extensively used in the DREAM model (Koller et al., 2007; Reeves et al., 2012), to calculate expected solar array degradation (Messenger et al., 2011) and to characterize relativistic electron flux rise times (Varotsou et al., 2008).

2.2. Data Analysis

The NS41 BDD-IIR data used in this study were downloaded from the United States Department of Commerce's NOAA website. Each normal file includes 2,520 records of duration 240 s, corresponding to one GPS-week of data. Each weekly file was examined, and excess records (almost always contained only “fill” values) were eliminated. Of the total of 1024 GPS-weeks during the lifetime of the mission, 31 were missing entirely, 3 included data for 1 day and 1 included data for two days. We used the data from the remaining 989 full weekly files in this study.

Each record includes 15 quantities identified as “differential flux” and the 15 energies at which the flux was evaluated. However, when plotted these quantities appear to be simple exponential functions of energy; they also do not agree with differential fluxes evaluated from the best-fitting parameter values reported in the same record, as described in Cayton et al. (2010). When multiplied by $p^2/2m_e$ the recorded values agree with the fluxes re-evaluated for the fitting parameters; when the re-evaluated differential fluxes, j , are divided by $p^2/2m_e$, the values of $j/p^2/2m_e$ agree with the recorded ones. Here p is the relativistic momentum and m_e is the electron rest mass and $p^2/2m_e$ is in units of MeV. The software that produced the version 1.09 space-weather files divides the evaluated differential flux by $p^2/2m_e$ before outputting the values. The 15 quantities in each record called “differential flux” are actually phase space densities in the units $\text{cm}^{-2} \text{s}^{-1} \text{sr}^{-1} \text{MeV}^{-2}$. Bona fide differential fluxes in units $\text{cm}^{-2} \text{s}^{-1} \text{sr}^{-1} \text{MeV}^{-1}$ may be calculated directly from the phase space densities reported in the version 1.09 space-weather files by multiplying each value by the appropriate energy factor $E(1 + E/2E_0)$, where E is the electron energy and E_0 is the electron rest mass energy, both in units of MeV. Channel counting rates and evaluated electron phase space densities were plotted; any observed glitches were eliminated; any out-of-phase coordinates, adjusted; any values containing system-test remnants were replaced by the average of the value before and the value after the affected one. Under normal conditions a system test was executed once each day and affected one of the 360 records for that day.

Electron phase space densities at 10 energies (0.6, 0.8, 1.0, 1.6, 2.0, 3.0, 4.0, 5.0, 6.0, and 8.0 MeV) were written into separate files for each crossing of 12 specific L -shell values (4.25, 4.50, 4.75, 5.00, 5.25, 5.50, 5.75, 6.00, 6.25, 6.50, 6.75, and 7.00). Here L is the McIlwain L value calculated using the International Geomagnetic Reference Field internal field and the Olson-Pfitzer quiet-time external field (Olson & Pfitzer, 1977). NS41 crosses each of the specified L -shells as many as 8 times each day. The phase space densities were then plotted as a function of time for each energy and L value to verify the absence of outliers and other peculiarities in the data. Electron differential fluxes were then calculated from these phase space densities by multiplying each by the corresponding energy factor (0.95225, 1.4262, 1.9785, 4.1049, 5.9139, 11.806, 19.656, 29.462, 41.225, and 70.622). Daily averaged fluxes were then compiled for each of the specified L -shells.

An example monthly summary plot of the daily average electron flux in the heart of the outer radiation belt at $L = 4.5$, is shown in Figure 1 for April 2010. To put the data into context the figure also shows relevant geophysical indices and solar wind parameters. Figure 1 shows (a–f) the electron flux at $E = 8.0, 6.0, 4.0, 2.0, 1.0$, and 0.6 MeV, respectively; (g) the solar wind speed (red trace) and Interplanetary Magnetic Field (IMF) B_z (black trace); (h) the Dst index (color coded) and solar wind pressure (black trace); and (i) the K_p (color coded) and AE (black trace) indices. The dotted lines in panels a–f represent the 1% exceedance level at each respective energy. The 1% exceedance level is exceeded for a number of days at each energy, with the peak values at each energy being the largest fluxes at that energy observed during the entire mission. These large fluxes are associated with several days of enhanced geomagnetic activity followed by a moderate geomagnetic storm that began on 5 April 2010.

To examine the behavior of the fluxes on a longer timescale we also plotted the electron fluxes for each year as a function of time for each energy and L value. Figure 2 shows one such summary plot of the daily average electron

NS41 BDD-IIR Electron Fluxes at L = 4.50

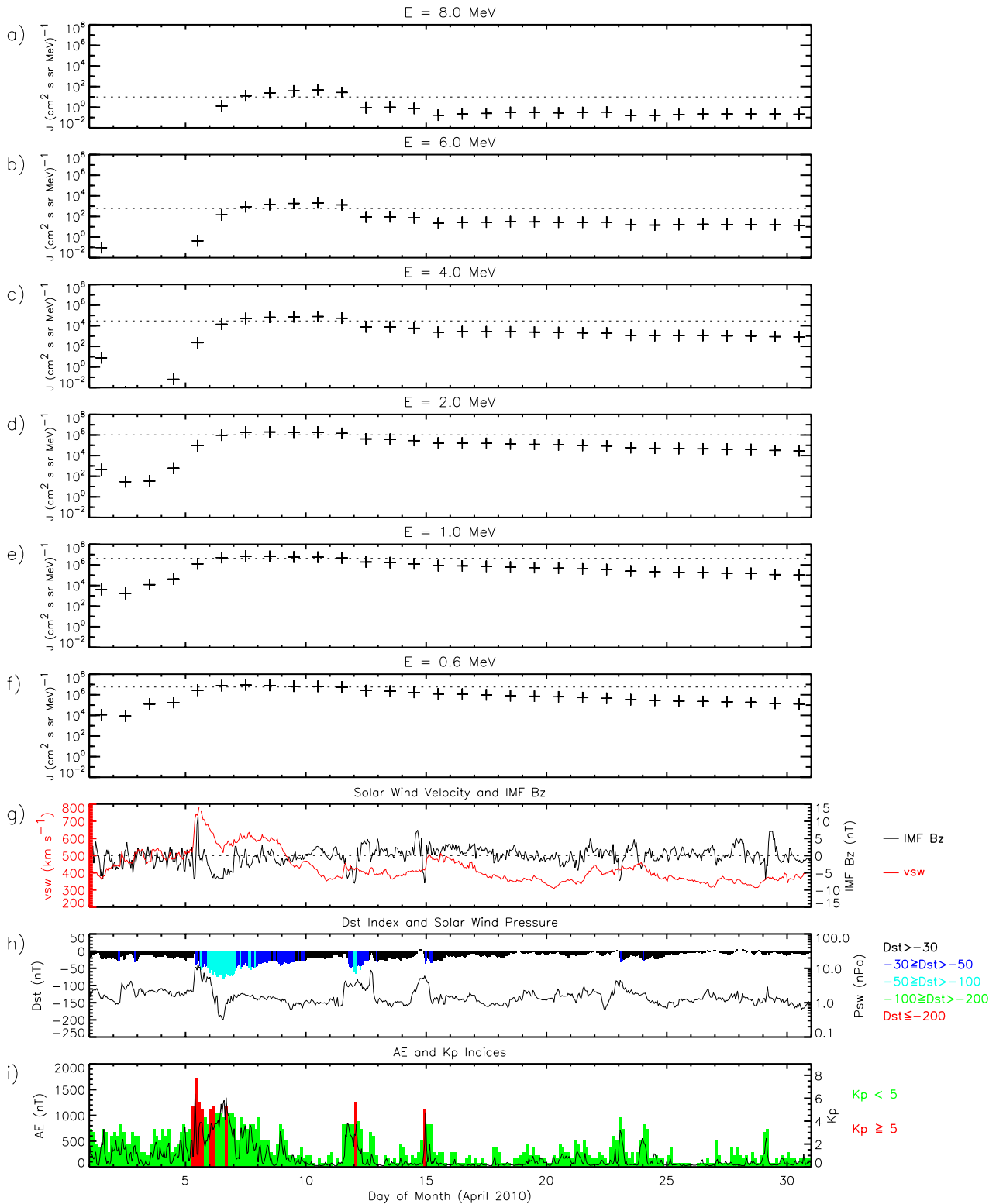


Figure 1. Summary plot of the NS41 Burst Detector Dosimeter IIR electron flux at $L = 4.5$ for April 2010. (a–f) The electron flux at $E = 8.0, 6.0, 4.0, 2.0, 1.0,$ and 0.6 MeV, respectively; (g) the solar wind speed (red trace) and Interplanetary Magnetic Field Bz (black trace); (h) the Dst index (color coded) and solar wind pressure (black trace); and (i) the Kp (color coded) and AE (black trace) indices. The dotted lines in panels a–f represent the 1% exceedance level at each respective energy.

NS41 BDD-IIR Electron Fluxes at L = 4.50

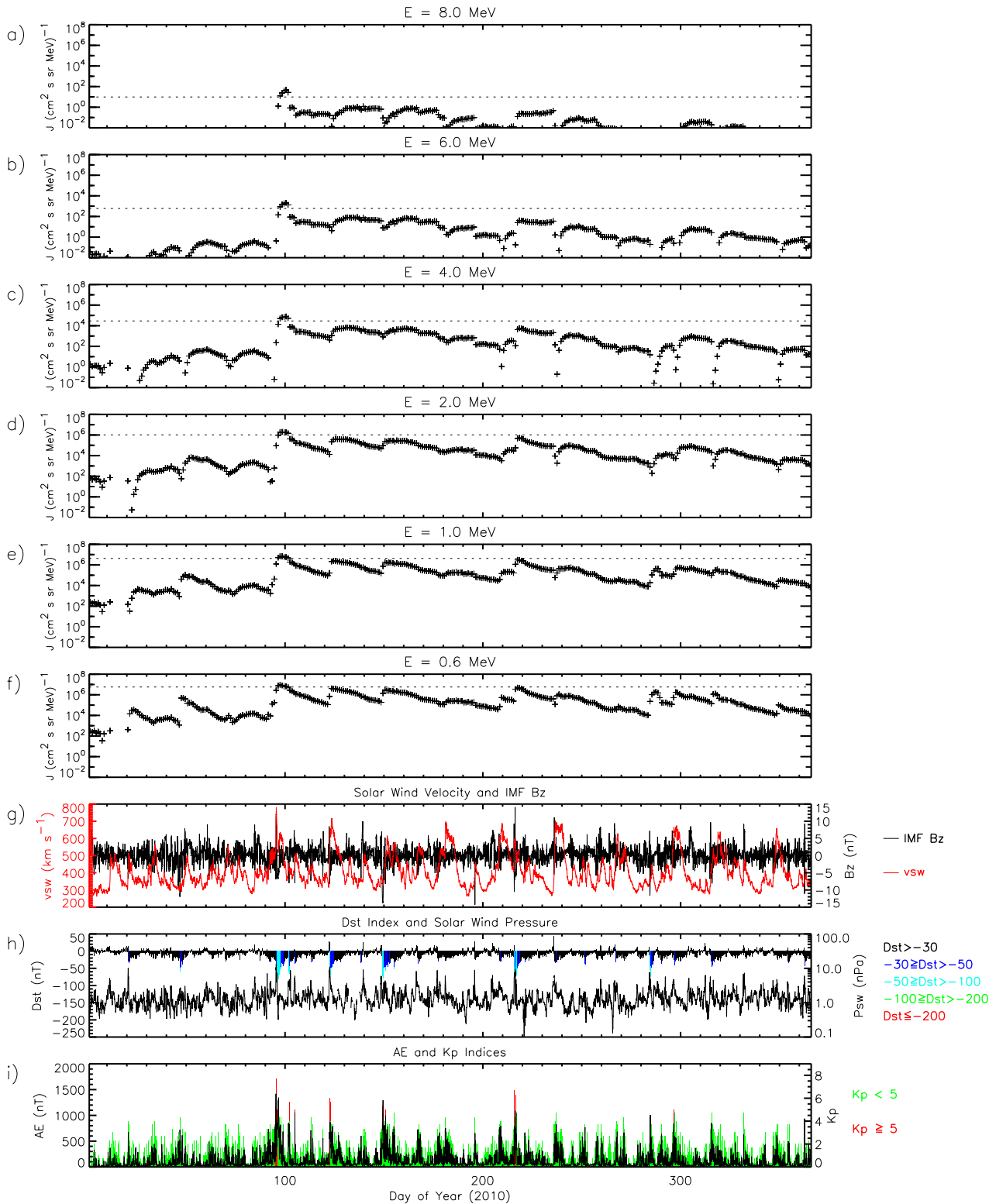


Figure 2. Summary plot of the NS41 Burst Detector Dosimeter IIR electron flux at $L = 4.5$ for 2010. (a–f) The electron flux at $E = 8.0, 6.0, 4.0, 2.0, 1.0,$ and 0.6 MeV, respectively; (g) the solar wind speed (red trace) and Interplanetary Magnetic Field B_z (black trace); (h) the Dst index (color coded) and solar wind pressure (black trace); and (i) the K_p (color coded) and AE (black trace) indices. The dotted lines in panels a–f represent the 1% exceedance level at each respective energy.

Table 1
Largest Electron Fluxes Observed at $E = 1.0, 2.0,$ and 4.0 MeV at $L = 4.5$

1.0 MeV		2.0 MeV		4.0 MeV	
Flux ($\text{cm}^2\text{ssrMeV})^{-1}$	Date	Flux ($\text{cm}^2\text{ssrMeV})^{-1}$	Date	Flux ($\text{cm}^2\text{ssrMeV})^{-1}$	Date
7.02×10^6	07 April 2010	1.98×10^6	08 April 2010	7.83×10^4	10 April 2010
6.67×10^6	20 January 2005	1.93×10^6	14 September 2005	7.28×10^4	09 April 2010
6.64×10^6	08 April 2010	1.87×10^6	07 April 2010	6.99×10^4	14 September 2005
6.21×10^6	14 September 2005	1.86×10^6	10 April 2010	6.59×10^4	08 April 2010
6.08×10^6	24 July 2004	1.85×10^6	09 April 2010	6.21×10^4	30 July 2004
5.88×10^6	18 May 2005	1.73×10^6	20 January 2005	6.10×10^4	21 September 2003
5.83×10^6	20 September 2003	1.72×10^6	21 September 2003	5.97×10^4	29 July 2004
5.80×10^6	19 January 2005	1.61×10^6	20 September 2003	5.88×10^4	22 September 2003
5.70×10^6	09 April 2010	1.59×10^6	22 September 2003	5.72×10^4	23 September 2003
5.68×10^6	16 April 2006	1.55×10^6	13 September 2005	5.53×10^4	31 July 2004

flux at $L = 4.5$ for 2010, in a similar format to Figure 1. At each energy the fluxes are characterized by relatively rapid increases followed by gradual decays lasting many days. The figure shows that in 2010 the 1% exceedance level was only exceeded during the April geomagnetic storm, although several other flux increases approached the 1% levels.

3. Statistics

The top 10 daily average fluxes of $E = 1.0, E = 2.0,$ and $E = 4.0$ MeV electrons at $L = 4.5,$ representative of the heart of the outer radiation belt, and $L = 6.5$ at higher magnetic latitudes on field lines that map to geostationary orbit, are tabulated in Tables 1 and 2 respectively. The largest daily average $E = 1.0, E = 2.0,$ and $E = 4.0$ MeV electron fluxes observed at $L = 4.5$ were $7.02 \times 10^6, 1.98 \times 10^6,$ and $7.83 \times 10^4 \text{ cm}^{-2} \text{ s}^{-1} \text{ sr}^{-1} \text{ MeV}^{-1}$ respectively, occurring on 7, 8 and 10 April 2010 respectively. Further out, at $L = 6.5,$ the largest fluxes of $E = 1.0, E = 2.0,$ and $E = 4.0$ MeV electrons were factors of 14, 14, and 18 lower for each energy respectively and all occurred on 10 April 2010. We note that the flux near the magnetic equator at $L = 6.5$ could be higher if the equatorial pitch angle distribution is peaked near 90° as electrons mirroring near the equator are not sampled at higher magnetic latitudes.

The distributions of the daily average electron fluxes at $L = 4.5, 5.0, 5.5,$ and 6.5 are shown in Figures 3a–3d respectively. The observed flux for any given exceedance probability decreases with increasing energy at each

Table 2
Largest Electron Fluxes Observed at $E = 1.0, 2.0,$ and 4.0 MeV at $L = 6.5$

1.0 MeV		2.0 MeV		4.0 MeV	
Flux ($\text{cm}^2\text{ssrMeV})^{-1}$	Date	Flux ($\text{cm}^2\text{ssrMeV})^{-1}$	Date	Flux ($\text{cm}^2\text{ssrMeV})^{-1}$	Date
5.20×10^5	10 April 2010	1.45×10^5	10 April 2010	4.32×10^3	10 April 2010
4.97×10^5	30 July 2004	1.21×10^5	30 July 2004	2.74×10^3	30 July 2004
3.89×10^5	11 April 2010	8.40×10^4	11 April 2010	1.50×10^3	11 April 2010
3.63×10^5	03 April 2008	7.20×10^4	03 April 2008	1.45×10^3	21 September 2005
3.29×10^5	12 May 2016	6.96×10^4	31 July 2004	1.41×10^3	31 July 2004
3.26×10^5	30 August 2018	6.73×10^4	05 August 2003	1.35×10^3	05 August 2003
3.24×10^5	09 April 2005	6.48×10^4	18 October 2017	1.33×10^3	15 November 2004
3.21×10^5	31 July 2004	6.43×10^4	12 May 2016	1.32×10^3	04 August 2004
3.18×10^5	18 October 2017	6.27×10^4	02 April 2008	1.19×10^3	18 December 2003
3.07×10^5	02 April 2008	6.02×10^4	30 August 2018	1.17×10^3	19 April 2006

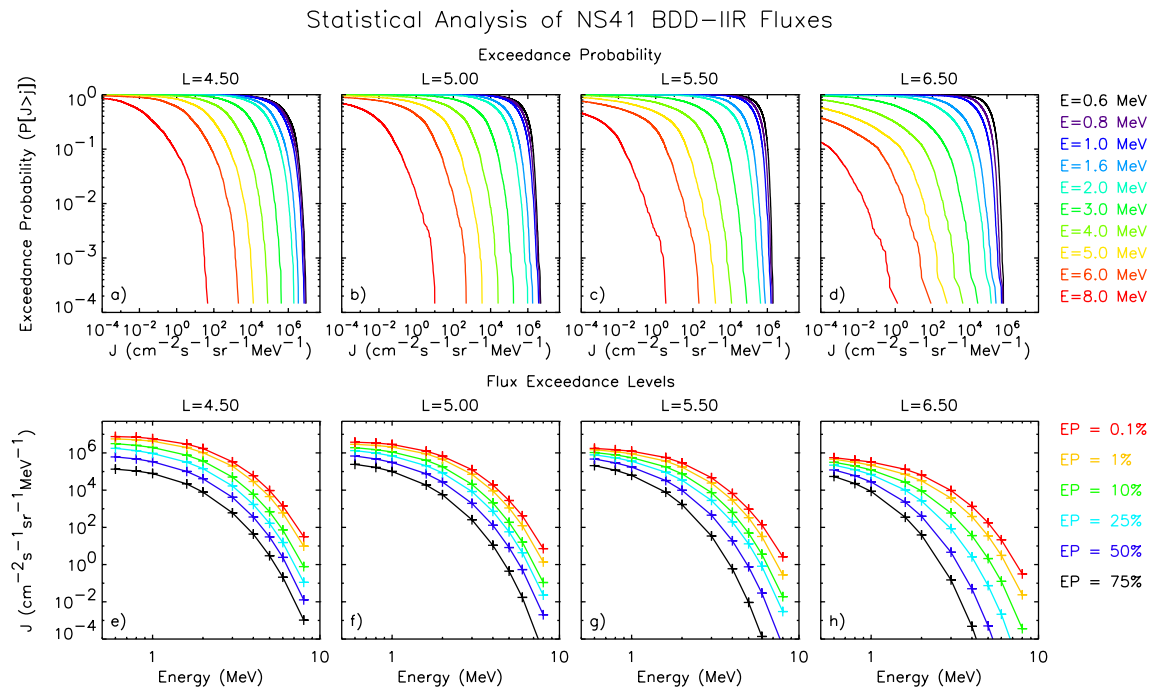


Figure 3. Plots of the exceedance probabilities for (a) $L = 4.5$, (b) $L = 5.0$, (c) $L = 5.5$, and (d) $L = 6.5$ for each electron energy and flux exceedance levels as a function of energy at (e) $L = 4.5$, (f) $L = 5.0$, (g) $L = 5.5$, and (h) $L = 6.5$.

value of L , as expected for relativistic electrons in the outer radiation belt where fluxes decrease with increasing energy. At any given energy and exceedance probability the observed flux also decreases with increasing L . There is also a tendency for the gradient of the exceedance probability for the top 1% of the fluxes to steepen with decreasing energy as can be seen from $E = 8.0$ through to $E = 0.6$ MeV, red to black traces, at $L = 6.5$ (Figure 3d). In other words, for exceedance probabilities less than 1%, there is only a small fractional increase in the flux at low energies compared to that at higher energies. The steepening also gets larger going to lower L . In the heart of the outer radiation belt, at $L = 4.5$, the largest observed fluxes cover over five orders of magnitude, ranging from $8.90 \times 10^6 \text{ cm}^{-2} \text{ s}^{-1} \text{ sr}^{-1} \text{ MeV}^{-1}$ at $E = 0.6$ MeV to $46 \text{ cm}^{-2} \text{ s}^{-1} \text{ sr}^{-1} \text{ MeV}^{-1}$ at $E = 8.0$ MeV. Further out, at $L = 6.5$, the largest fluxes are factors of 14 and 34 lower at $E = 0.6$ and 8.0 MeV respectively.

The fluxes corresponding to selected exceedance probabilities at $L = 4.5, 5.0, 5.5$, and 6.5 are shown in Figures 3e–3h respectively. The flux for a given exceedance probability decreases with increasing energy. At $L = 4.5$ the 1% exceedance level ranges from $5.67 \times 10^6 \text{ cm}^{-2} \text{ s}^{-1} \text{ sr}^{-1} \text{ MeV}^{-1}$ at $E = 0.6$ MeV to $9.78 \text{ cm}^{-2} \text{ s}^{-1} \text{ sr}^{-1} \text{ MeV}^{-1}$ at $E = 8.0$ MeV. Further out, at $L = 6.5$, the 1% exceedance levels are factors of 12 and 409 lower at $E = 0.6$ and 8.0 MeV respectively.

The fluxes for selected exceedance levels are shown as a function of L for four selected energies in Figure 4. The median flux of relativistic electrons in the energy range $0.6 \leq E \leq 2.0$ MeV peaks at $L = 4.75$. However, for exceedance levels below 10%, for any given energy, the fluxes peak at $L = 4.25$, the inner limit of the observations, and decrease with increasing L .

4. Extreme Value Analysis

The main objective of this study is to determine the 1 in 10 and 1 in 100 year daily average electron flux for the specified energies and L shells. Since daily averages are available and to compare with our previous studies (Meredith et al., 2015, 2016a, 2016b, 2017), we use the exceedances over a high threshold approach (Dey & Das, 2016; Thomson et al., 2011). For this approach, also known as the Peaks Over Threshold method, the appropriate distribution function is the generalized Pareto distribution (GPD), first introduced by Picklands (1975). This model assumes that the underlying physics is similar during extreme events. For example, it assumes that an extremely rare event doesn't occur with a completely different set of characteristics, not seen before. This assumption is likely to be valid for the outer radiation belt studied here, but would not necessarily hold for the inner radiation belt (e.g., Shprits et al., 2011). This approach has been used successfully in many fields to estimate, for example, extremes of rainfall (e.g., Li et al., 2005),

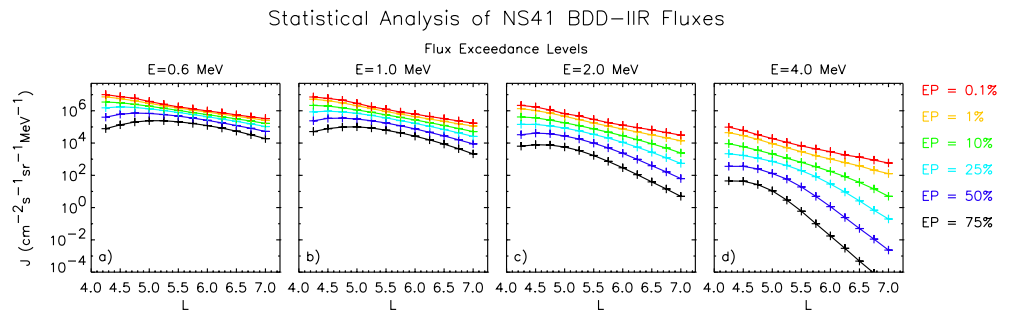


Figure 4. Plots of the flux exceedance levels as a function of L for (a) $E = 0.6$, (b) $E = 1.0$, (c) $E = 2.0$, and (d) $E = 4.0$ MeV electrons.

surface temperature (e.g., Nogaj et al., 2006), geomagnetic storm events (Tsubouchi & Omura, 2007), wind speed (e.g., Della-Marta et al., 2009), geomagnetic activity (Thomson et al., 2011), storm surge (e.g., Tebaldi et al., 2012), hurricane damage (Dey & Das, 2016), and the probability of Carrington-like solar flares (Elvidge & Angling, 2018).

The threshold at each energy and L should be low enough to include a meaningful number of data points and high enough to capture the behavior of the tail of the distribution. Based on experience analyzing other satellite data sets (e.g., Meredith et al., 2015, 2017), for each energy and L we set the threshold at the 1% exceedance level. We declustered the data by assuming a cluster to be active until three consecutive daily average values fell below the chosen threshold. We then fit the GPD (Coles, 2001; Picklands, 1975) to the cluster maxima for each specified energy and L shell using the `ismev` library routine `gpd.fit` provided in the R statistical package (R Foundation for Statistical Computing, 2008). The GPD may be written as:

$$G(y) = 1 - \left(1 + \frac{\xi y}{\sigma}\right)^{-\frac{1}{\xi}} \quad (1)$$

where $y = (x - u)$ are the exceedances, x are the cluster maxima above the chosen threshold, u , ξ is the shape parameter and σ the scale parameter (Coles, 2001). The sign of the shape parameter provides important information on the behavior of tail of the distribution. If ξ is positive the distribution has no upper limit whereas if ξ is negative the distribution has an upper bound. The level, x_N , which is exceeded on average once every N years may be expressed in terms of ξ and σ as:

$$x_N = u + \frac{\sigma}{\xi} \left((N n_d n_c / n_{tot})^\xi - 1 \right) \quad (2)$$

where n_c is the number of clusters, n_{tot} is the total number of data points and $n_d = 365.25$ is the average number of days in any given year (Coles, 2001).

5. Results

To demonstrate the method used we first show the results for $E = 0.6$ MeV electrons at $L = 4.5$. The $E = 0.6$ MeV daily average electron flux is shown as a function of time in Figure 5a. The 1% exceedance level of $5.67 \times 10^6 \text{ cm}^{-2} \text{ s}^{-1} \text{ sr}^{-1} \text{ MeV}^{-1}$, chosen as the threshold for the extreme value analysis, is shown as the dotted line and the cluster maxima are coded red. A trace of the 27-day average sunspot number is shown in Figure 5b. The largest fluxes of $E = 0.6$ MeV electrons at $L = 4.5$ are largely seen from 2003–2008 and 2015–2018 during the declining phases of solar cycles 23 and 24 respectively, with lower fluxes typically being seen around the solar minima and solar maxima.

The scale and shape parameters for the fit to the cluster maxima of $E = 0.6$ MeV electrons at $L = 4.5$ are determined to be $(1.5 \pm 0.01) \times 10^6$ and -0.39 ± 0.08 respectively. The shape parameter is negative, suggesting that the flux of 0.6 MeV electrons at $L = 4.5$ tends to a limiting value. To assess the quality of the fitted GPD model we compare the empirical and modeled probabilities and quantiles (Coles, 2001). Figure 6a shows the probability plot for the cluster maxima of the $E = 0.6$ MeV electron flux. Here we plot the modeled probability, $G(y)$ against the empirical probability, that X exceeds some value x given that it already exceeds a threshold u . The best fit

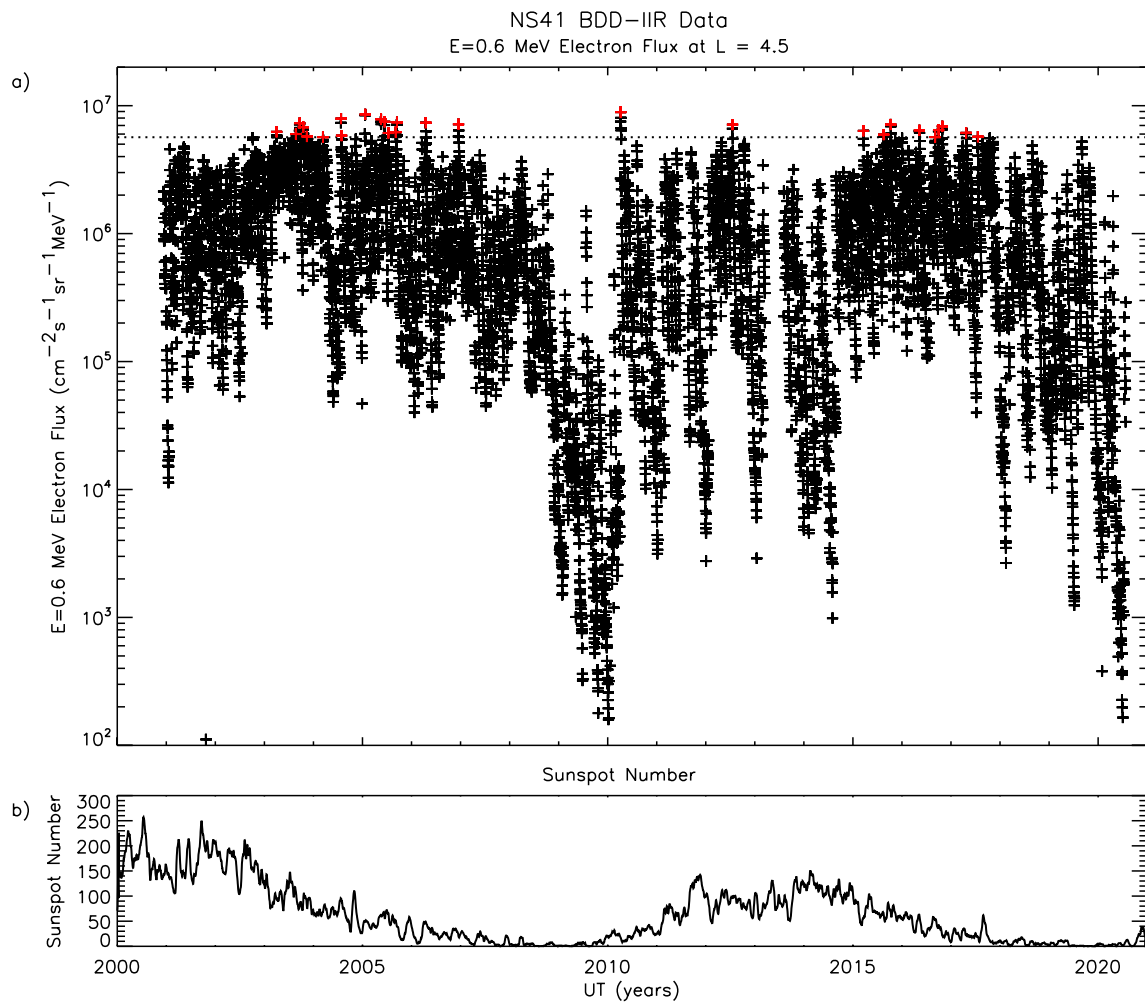


Figure 5. Plot of the $E = 0.6$ MeV daily average electron flux as a function of time at $L = 4.5$. (a) The 1% exceedance level, chosen as the threshold for the extreme value analysis, is shown as a dotted line and the cluster maxima are coded red. (b) Trace of the sunspot number as a function of time.

straight line to the data points is shown in blue and has a correlation coefficient of 0.994. Figure 6b shows the quantile plot for the cluster maxima of the $E = 0.6$ MeV electron flux. Here we plot the modeled fluxes against the empirical fluxes. The best fit straight line is again shown in blue and has a correlation coefficient of 0.992. The fact that both fits are approximately linear suggests that the generalized Pareto model is a good method for modeling the exceedances (e.g., Coles, 2001).

Figure 6c shows the exceedance probability of the cluster maxima above the threshold value of $5.67 \times 10^6 \text{ cm}^{-2} \text{ s}^{-1} \text{ sr}^{-1} \text{ MeV}^{-1}$, ($P[J > j | J > u]$) (black symbols), together with the maximum likelihood fit (blue line). Figure 6d shows the flux that is exceeded on average once every N years as a function of N for the declustered $E = 0.6$ MeV electron flux. The 1 in N year return level determined from Equation 2 is shown as the solid blue line and the symbols represent the experimental return levels. The 95% confidence interval of the 1 in N year return levels are shown as the dotted blue lines. The 1 in 10, 1 in 50, and 1 in 100 year $E = 0.6$ MeV electron fluxes at $L = 4.5$ are $(8.20 \pm 0.49) \times 10^6$, $(8.85 \pm 0.81) \times 10^6$, and $(9.03 \pm 0.93) \times 10^6 \text{ cm}^{-2} \text{ s}^{-1} \text{ sr}^{-1} \text{ MeV}^{-1}$, where the quoted errors represent the 95% confidence limits.

We repeated the analysis for each electron energy at each value of L and determined the corresponding 1 in N year fluxes. The return levels are shown as a function of energy at $L = 4.5, 5.0, 5.5,$ and 6.5 in Figures 7a–7d respectively. The 1 in N year fluxes decrease with increasing energy and L . At $L = 4.5$ there is very little difference between the 1 in 10 and 1 in 100 year events (Figure 7a). However, further out, there is an increasing tendency for more variation in the 1 in 10 and 1 in 100 year events, particularly at higher energies, with the threshold at which the variability increases decreasing with increasing L (Figures 7b–7d). Specifically, at $L = 4.5$ (Figure 7a), the 1

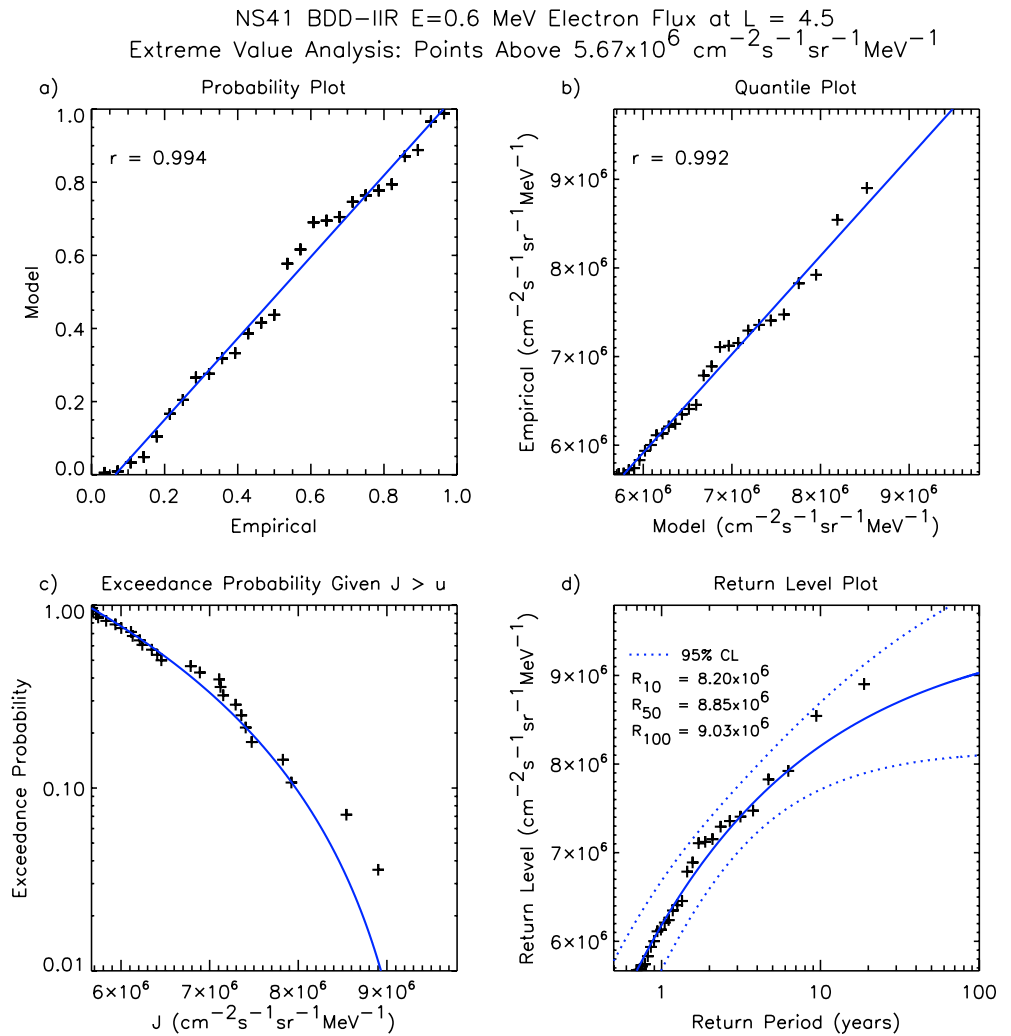


Figure 6. Extreme value analysis for the $E = 0.6$ MeV daily average electron flux at $L = 4.5$. (a) Probability plot, (b) quantile plot, (c) the exceedance probability given $J > u$, and (d) the return level plot.

in 10 year flux (black line) ranges from $8.2 \times 10^6 \text{ cm}^{-2} \text{ s}^{-1} \text{ sr}^{-1} \text{ MeV}^{-1}$ at $E = 0.6$ MeV to $33 \text{ cm}^{-2} \text{ s}^{-1} \text{ sr}^{-1} \text{ MeV}^{-1}$ at $E = 8.0$ MeV, with the 1 in 100 year event (red line) being a factor of 1.1–1.7 larger than the corresponding 1 in 10 year event. Further out, at $L = 6.5$ (Figure 7c), the 1 in 10 year flux (black line) ranges from $6.2 \times 10^5 \text{ cm}^{-2} \text{ s}^{-1} \text{ sr}^{-1} \text{ MeV}^{-1}$ at $E = 0.6$ MeV to $0.48 \text{ cm}^{-2} \text{ s}^{-1} \text{ sr}^{-1} \text{ MeV}^{-1}$ at $E = 8.0$ MeV, with the 1 in 100 event being a factor of 1.1–13 times larger than the corresponding 1 in 10 year event.

The shape parameter from the extreme value analysis is shown as a function of energy at $L = 4.5, 5.0, 5.5,$ and 6.5 in Figures 7e–7h respectively. In the heart of the outer radiation belt, at $L = 4.5$ (Figure 7e), the shape parameter is robustly negative, with the maximum of the 95% confidence interval lying below 0, at energies in the range $0.6 \leq E \leq 2.0$ MeV, suggesting that the electron fluxes in this region and at these energies are bounded and tend to a limiting value. At higher energies the shape parameter remains largely negative in this region although the error bars include positive values, making it difficult to be conclusive about the whether the fluxes are bounded or unbounded at $E \geq 3$ MeV. Similar behavior is observed at $L = 4.25$ and 4.75 (not shown). Moving out in L , at $L = 5.0$ (Figure 7f) and $L = 5.25$ (not shown), the shape parameter is mostly negative, but with error bars that includes both positive and negative values, again making it difficult to be conclusive about whether the fluxes are bounded or unbounded in this region. Further out there is an increasing tendency for the shape parameter to become robustly positive at higher energies from $E \geq 4.0$ MeV at $L = 5.5$ (Figure 7g), from $E \geq 3$ MeV at $L = 6.5$ (Figure 7h) and from $E \geq 1$ MeV at $L = 7.0$ (not shown). This suggests that the relativistic electron fluxes in these regions and at these energies have no upper bound. Interestingly, the shape parameter is robustly negative for the

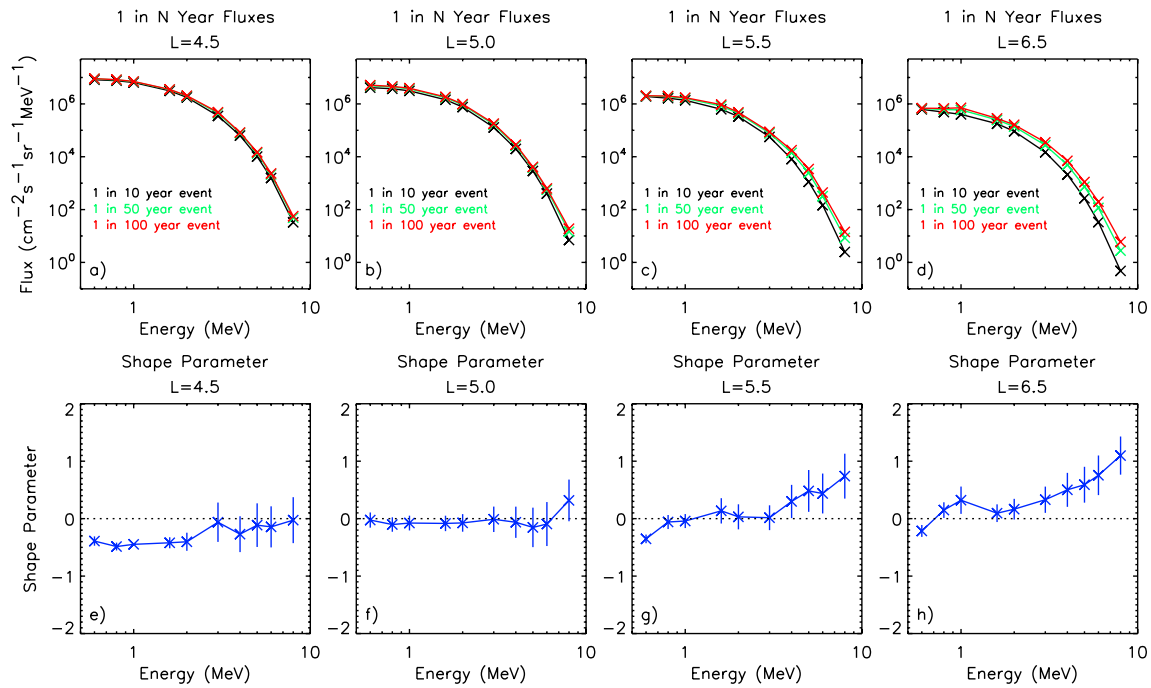


Figure 7. Plots of the 1 in N year electron flux as a function of energy for $N = 10$ (black trace and symbols), 50 (green trace and symbols), and 100 years (red trace and symbols) for (a) $L = 4.5$, (b) $L = 5.0$, (c) $L = 5.5$, and (d) $L = 6.5$ and the shape parameter as a function of energy for (e) $L = 4.5$, (f) $L = 5.0$, (g) $L = 5.5$, and (h) $L = 6.5$.

$E = 0.6$ MeV electrons in this region (Figures 7g and 7h), suggesting that the 0.6 MeV electron fluxes also have an upper bound at larger L all the way out to $L = 7.0$ (not shown).

The 1 in 10, 1 in 50, and 1 in 100 year fluxes are summarized as a function of L for each energy in Figures 8a–8c respectively. The 1 in 100 year flux of $E = 0.6$ MeV electrons decreases with increasing L ranging from to 1.2×10^7 cm⁻² s⁻¹ sr⁻¹ MeV⁻¹ at $L = 4.25$ to 3.8×10^5 cm⁻² s⁻¹ sr⁻¹ MeV⁻¹ at $L = 7.00$, and are factors of 1.1 times the corresponding 1 in 10 year flux. At higher energies, the 1 in 100 year flux of $E = 2.0$ MeV electrons ranges from to 3.0×10^6 cm⁻² s⁻¹ sr⁻¹ MeV⁻¹ at $L = 4.25$ to 1.1×10^5 cm⁻² s⁻¹ sr⁻¹ MeV⁻¹ at $L = 7.00$ and are factors of 1.3 and 2.2 larger than the corresponding 1 in 10 year fluxes respectively.

6. Discussion

Some of the largest daily average fluxes encountered during the entire mission were observed during the 6 April 2010 geomagnetic storm (Figure 1). This was a relatively moderate geomagnetic storm with a minimum Dst

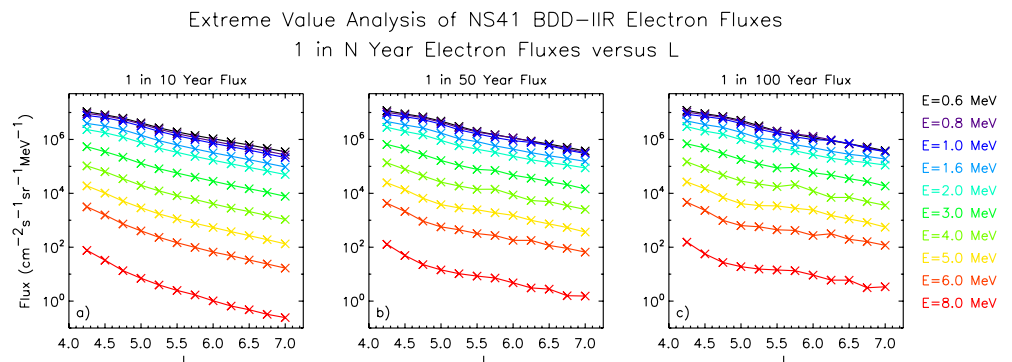


Figure 8. Plots of the 1 in N year electron flux as a function of L for each energy (color-coded) for (a) $N = 10$ years, (b) $N = 50$ years, and (c) $N = 100$ years.

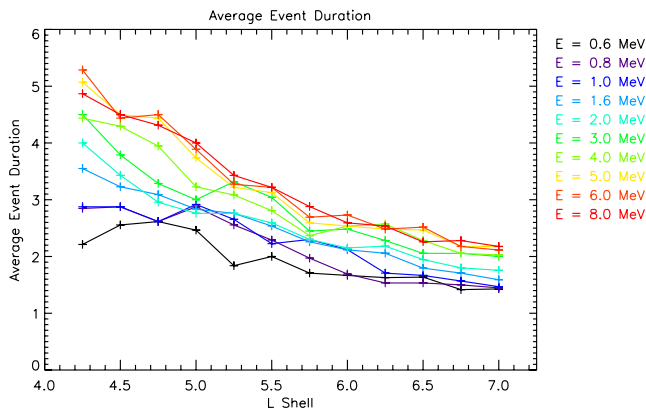


Figure 9. Plots of the average event duration as a function of L for each energy (color-coded).

of -81 nT at 14:00 UT on 6 April 2010. The recovery phase of this storm lasted for approximately 5 days, the first 4 days of which were associated with enhanced geomagnetic activity. Interestingly, the relativistic electron fluxes at $L = 4.5$ had started to rise from 2 April, prior to the arrival of the geomagnetic storm due to a period of IMF Bz fluctuating about zero and enhanced geomagnetic activity as monitored by the AE index. The largest daily averaged fluxes of relativistic electrons in the heart of the outer radiation belt at $L = 4.5$ at each energy were observed during this storm. Here the flux peaks ranged from $8.9 \times 10^6 \text{ cm}^{-2} \text{ s}^{-1} \text{ sr}^{-1} \text{ MeV}^{-1}$ at $E = 0.6$ MeV to $46 \text{ cm}^{-2} \text{ s}^{-1} \text{ sr}^{-1} \text{ MeV}^{-1}$ at $E = 8.0$ MeV on the 7 and 10 April respectively. The large flux levels were also sustained, remaining above the 1% exceedance level for 5 days. Further out, at $L = 6.5$, the largest daily average fluxes were observed at all energies in the range $0.8 \leq E \leq 8.0$ MeV, ranging from $6.0 \times 10^5 \text{ cm}^{-2} \text{ s}^{-1} \text{ sr}^{-1} \text{ MeV}^{-1}$ at $E = 0.8$ MeV to $1.36 \text{ cm}^{-2} \text{ s}^{-1} \text{ sr}^{-1} \text{ MeV}^{-1}$ at $E = 8.0$ MeV. Here, the high flux level were sustained for a shorter period of time, remaining above the 1% level for 2 days.

The largest internal charging currents observed by the top, middle and bottom plates of the SURF instrument on Giove-A between December 2005 and January 2016 also occurred during this event, both at $L^* = 4.75$ near the heart of the outer radiation belt and at $L^* = 6.0$ on field lines that map out close to geostationary orbit (Meredith et al., 2016b). This suggests that the largest observed internal charging currents recorded by each of the SURF plates in these two locations are rarer than would be expected based on the original statistics, with, for example, the empirical return period being of the order of 20 years as opposed to 8.5 years estimated in the original study.

In this study we have focused on the 1 in 10 and 1 in 100 year daily average relativistic electron fluxes as a function of energy and L . However, the duration of the enhanced fluxes associated with the largest events are also important, since charge deposited on insulators and ungrounded conductors builds up over time. Figure 9 shows the average time the flux exceeds the 1% exceedance level for each of the cluster maxima for each energy (color-coded) as a function of L . At $L = 4.5$ the average event duration increases with increasing energy from 2.5 days at 0.6 MeV to 4.4 days at the highest energies. The same trend is seen at larger L , for example, $L = 6.5$, but the average duration is smaller ranging from 1.4 days at $E = 0.6$ MeV to 2.5 days at $E = 8.0$ MeV. Although we are not fitting decay timescales the data indicate that, over the range of energies and L sampled, the timescale for loss is generally smaller at lower energies and higher L .

The conclusion that the fluxes tend to a limiting value in the region $4.25 \leq L \leq 4.75$ at energies in the range is $0.6 \leq E \leq 2.0$ MeV is consistent with the findings from a similar analysis of the INTEGRAL IREM data (Meredith et al., 2017). However, the latter study also concluded that the relativistic electrons in this energy range tended to limiting values out to $L^* = 6.0$. Unfortunately, our study does not throw any definitive light on the behavior of the relativistic electron fluxes in the energy range $0.6 \leq E \leq 2.0$ MeV beyond $L \geq 5.0$ due to the fact that the shape parameter is mostly close to zero with error bars encompassing both positive and negative values. However, at higher energies and high L the shape parameter is robustly positive, suggesting the fluxes are unbounded at high energy and high L .

It is hard to understand why the fluxes at the higher energies and high L , for example, $E > 3$ MeV at $L = 6.5$, have no upper bound when the plots of the 1 in N year fluxes are so smooth and the 1 in N year flux levels at the higher energies are orders of magnitude lower than the corresponding flux levels at 0.6 MeV, which are bounded. One possibility is that fluxes approaching the limiting value are extremely rare at higher energy and L , highlighting the inherent difficulty in using 20 years of data to infer the presence or absence of an upper limit which may typically not be reached for 100 years or more. Another possible reason for the difference is that the instrument samples higher L shells at higher magnetic latitudes and there could be some variation in anisotropy that is not captured at higher energy and L .

When the shape parameter is negative, the limiting value, x_L , can be calculated for any given energy and L and is given by

$$x_L = u - \frac{\sigma}{\xi} \quad (3)$$

Table 3
1 in 10 Year, 1 in 100 Year and Limiting Fluxes at L = 4.5 and L = 6.5

Energy (MeV)	L = 4.5			L = 6.5		
	1 in 10 yr Flux (cm ² ssrMeV) ⁻¹	1 in 100 yr Flux (cm ² ssrMeV) ⁻¹	Limiting Flux (cm ² ssrMeV) ⁻¹	1 in 10 yr Flux (cm ² ssrMeV) ⁻¹	1 in 100 yr Flux (cm ² ssrMeV) ⁻¹	Limiting Flux (cm ² ssrMeV) ⁻¹
0.6	8.2 × 10 ⁶	9.0 × 10 ⁶	9.6 × 10 ⁶	6.2 × 10 ⁵	6.9 × 10 ⁵	7.9 × 10 ⁵
0.8	7.6 × 10 ⁶	8.3 × 10 ⁶	8.6 × 10 ⁶	4.9 × 10 ⁵	6.8 × 10 ⁵	–
1.0	6.4 × 10 ⁶	7.1 × 10 ⁶	7.4 × 10 ⁶	4.0 × 10 ⁵	7.1 × 10 ⁵	–
1.6	3.1 × 10 ⁶	3.5 × 10 ⁶	3.8 × 10 ⁶	1.8 × 10 ⁵	2.8 × 10 ⁵	–
2.0	1.8 × 10 ⁶	2.0 × 10 ⁶	2.2 × 10 ⁶	9.2 × 10 ⁴	1.6 × 10 ⁵	–
3.0	3.5 × 10 ⁵	4.8 × 10 ⁵	–	1.5 × 10 ⁴	3.5 × 10 ⁴	–
4.0	6.3 × 10 ⁴	8.3 × 10 ⁴	–	2.1 × 10 ³	7.0 × 10 ³	–
5.0	1.0 × 10 ⁴	1.5 × 10 ⁴	–	2.7 × 10 ²	1.1 × 10 ³	–
6.0	1.6 × 10 ³	2.3 × 10 ³	–	3.4 × 10 ¹	2.0 × 10 ²	–
8.0	3.3 × 10 ¹	5.6 × 10 ¹	–	4.8 × 10 ⁻¹	6.0 × 10 ⁰	–

The limiting fluxes as a function of energy at $L = 4.5$ and $L = 6.5$ are tabulated in Table 3, together with the 1 in 10 and 1 in 100 year fluxes. Here we only tabulate the limiting fluxes when the upper limit of 95% confidence interval of the shape parameter is negative. At $L = 4.5$ the limiting fluxes lie in the range $9.6 \times 10^6 \text{ cm}^{-2} \text{ s}^{-1} \text{ sr}^{-1} \text{ MeV}^{-1}$ at $E = 0.6 \text{ MeV}$ to $2.2 \times 10^6 \text{ cm}^{-2} \text{ s}^{-1} \text{ sr}^{-1} \text{ MeV}^{-1}$ at $E = 2.0 \text{ MeV}$ and are up to factors of 1.26 and 1.07 times larger than the corresponding 1 in 10 and 1 in 100 year fluxes. Further out, at $L = 6.5$ the limiting flux of $E = 0.6 \text{ MeV}$ electrons is $7.9 \times 10^5 \text{ cm}^{-2} \text{ s}^{-1} \text{ sr}^{-1} \text{ MeV}^{-1}$ and is a factor of 1.27 and 1.14 times larger than the corresponding 1 in 10 and 1 in 100 year fluxes.

It is interesting to note that when the fluxes tend to limiting values the 1 in 100 year flux or, indeed, the limiting flux is not significantly larger than the 1 in 10 year flux. For example, at $L = 4.5$ the limiting flux is between 1.1 and 1.3 times larger than the 1 in 10 year flux. This is not the case when the fluxes are unbounded and the differences between the 1 in 10 and 1 in 100 year fluxes are much greater. For example, at $L = 6.5$ the 1 in 100 year fluxes of $E = 4.0$ and $E = 6.0 \text{ MeV}$ electrons are factors of 3.6 and 5.9 times higher than the corresponding 1 in 10 year events. A major consequence of this type of behavior is that there are a much larger number of occurrences of fluxes approaching the 1 in 100 year flux for the bounded compared to unbounded cases. This is demonstrated in Table 4 where we tabulate the number of times the daily average flux is within a factor of two of the corresponding 1 in 100 year flux. In the table the bounded cases are printed in bold, the undetermined case in italic and the unbounded cases in normal font. At $L = 4.5$, where the daily average $E = 1.0 \text{ MeV}$ fluxes are bounded, the daily average $E = 1.0 \text{ MeV}$ flux lies within a factor of two of the 1 in 100 year flux on 126 days. Further out, at $L = 6.5$, where the corresponding fluxes are unbounded, the daily average $E = 1.0 \text{ MeV}$ flux lies within a factor of two of the 1 in 100 year flux on only 12 days. Thus, the behavior of the tail of the distribution is important when not only determining the 1 in 100 year flux but also in determining the number of times the fluxes approach within a given factor of the 1 in 100 year flux.

It is informative to compare the results of our study with the IRENE AE9 radiation environment model (Johnston et al., 2014; O'Brien et al., 2018). Figure 10a shows a comparison between the 99th percentile of the BDD-IIR fluxes at $L = 4.25$ as a function of energy (red trace and symbols) with the 99th percentile of version 1.5 of the IRENE AE9 radiation environment model for equatorial MEO orbit at 20,200 km (black trace and symbols). The results are largely in extremely good agreement both in magnitude and spectral shape for a wide range of energies from 0.6 to 6.0 MeV. This also gives us confidence in the measured fluxes at higher energies, in particular, up to 6.0 MeV. A significant departure is seen at $E = 8.0 \text{ MeV}$ with the 99th percentile of the AE9 model being a factor of 8 times greater than the 99th percentile of the BDD-IIR fluxes. The fact that the observed fluxes are less than those in AE9 at $E = 8.0 \text{ MeV}$ suggests that the issue is not associated with background counting issues in the BDD-IIR. It could be due to background counting issues in the data used to determine the AE9 model, especially given the fact that the gradient in the AE9 fluxes becomes less steep around 6.0 MeV. Alternatively, it could be due to the methods used to fit the data. Determining the reason warrants further investigation but is beyond the scope of the present study.

In 2017, we conducted an extreme value analysis using ~14 years of data from the Radiation Environment Monitor on board the INTEGRAL spacecraft (Meredith et al., 2017). The 1 in 100 year event at $L = 4.25$ ranged

Table 4
Number of Times the Daily Average Flux Is Within a Factor of Two of the Corresponding 1 in 100 Year Flux

<i>L</i>	<i>E</i> = 0.6 MeV	<i>E</i> = 0.8 MeV	<i>E</i> = 1.0 MeV	<i>E</i> = 2.0 MeV	<i>E</i> = 4.0 MeV	<i>E</i> = 6.0 MeV	<i>E</i> = 8.0 MeV
4.25	147	148	134	25	13	6	3
4.50	195	144	126	67	24	12	4
4.75	148	116	99	49	25	14	0
5.00	159	103	98	52	27	8	0
5.25	447	207	124	55	20	8	0
5.50	743	205	114	13	5	2	0
5.75	742	114	47	8	2	0	0
6.00	677	100	19	4	2	0	0
6.25	570	91	22	3	1	0	0
6.50	339	57	12	2	1	0	0
6.75	372	63	15	3	1	0	0
7.00	406	57	13	3	0	0	0

Note. Bounded cases in bold font, unbounded cases in normal font and undetermined cases in italic font.

from $1.5 \times 10^7 \text{ cm}^{-2} \text{ s}^{-1} \text{ sr}^{-1} \text{ MeV}^{-1}$ at $E = 0.69 \text{ MeV}$ to $6.4 \times 10^5 \text{ cm}^{-2} \text{ s}^{-1} \text{ sr}^{-1} \text{ MeV}^{-1}$ at $E = 2.05 \text{ MeV}$. These findings can be compared with the new results from the NS41 BDD-IIR instrument. The 1 in 100 year fluxes determined from the BDD-IIR data at $L = 4.25$ range from $1.2 \times 10^7 \text{ cm}^{-2} \text{ s}^{-1} \text{ sr}^{-1} \text{ MeV}^{-1}$ at $E = 0.6 \text{ MeV}$ to $3.0 \times 10^6 \text{ cm}^{-2} \text{ s}^{-1} \text{ sr}^{-1} \text{ MeV}^{-1}$ at $E = 2.0 \text{ MeV}$ (Figure 10b). The results are in good agreement at 0.8 and 1 MeV but the INTEGRAL results are about a factor of five lower at 1.6 and $\sim 2 \text{ MeV}$.

One of the largest geomagnetic storms of the last 20 years was the Halloween storm in 2003, with a Dst minimum of -383 nT on 30th October at 22:00 UT. Following the storm a new outer radiation belt formed at low L , peaking in the slot region inside $L = 3.0$ (Baker et al., 2004; Horne et al., 2005). This event is not associated with large fluxes of relativistic electrons as observed by NS41, either toward the edge of the outer radiation belt or in the usual position of the heart of the radiation belt. This event serves to show that the 1 in 10 and 1 in 100 year fluxes in MEO and GEO are not related to the most extreme storms as monitored by the Dst index. This is consistent with Horne et al. (2018) who found that satellites at GEO are more likely to be at risk from a fast solar wind stream event than from a major storm. In such storms the outer radiation belt often reforms inside MEO and is depleted at higher L values. Relativistic electrons during this type of extreme storm would not pose a risk

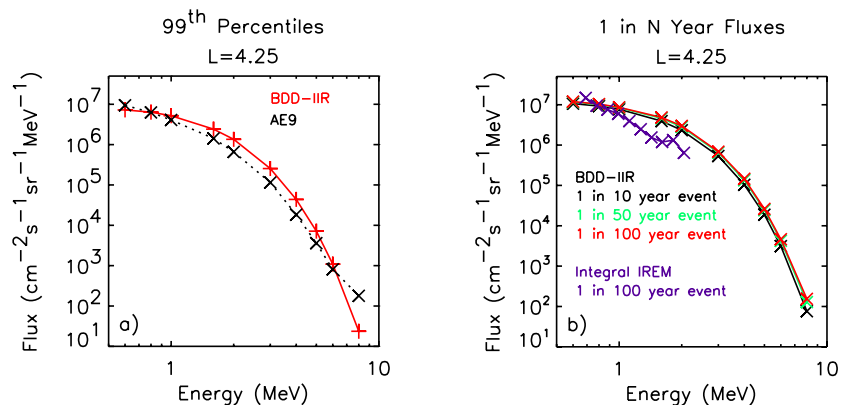


Figure 10. (a) Plot of the 99th percentile of the Burst Detector Dosimeter IIR fluxes at $L = 4.25$ (red trace and symbols) and the 99th percentile of the IRENE AE9 fluxes for a 20,200 km equatorial orbit (black trace and symbols) as a function of energy. (b) Plot of the 1 in N year electron flux at $L = 4.25$ as a function of energy for $N = 10$ (black trace and symbols), 50 (green trace and symbols), and 100 years (red trace and symbols), together with the 1 in 100 year electron flux determined from INTEGRAL IREM (purple trace and symbols).

to satellites in MEO or GEO. However, the situation would be different for satellites in the slot region, such as the O3B satellites. The slot region is usually devoid of relativistic electrons but, during such severe storms, can become elevated and remain elevated for weeks or even months (Baker et al., 2007), significantly increasing the risk to satellites operating in this region.

7. Conclusions

We have conducted an extreme value analysis of the relativistic electron flux in GPS orbit as a function of energy and L using data from the BDD-IIR instrument on the US NS41 satellite. Our principal results are as follows:

1. The 1 in 10 year flux at $L = 4.5$, near the heart of the outer radiation belt, decreases with increasing energy ranging from $8.2 \times 10^6 \text{ cm}^{-2} \text{ s}^{-1} \text{ sr}^{-1} \text{ MeV}^{-1}$ at $E = 0.6 \text{ MeV}$ to $33 \text{ cm}^{-2} \text{ s}^{-1} \text{ sr}^{-1} \text{ MeV}^{-1}$ at $E = 8.0 \text{ MeV}$. The 1 in 100 year event exhibits a similar trend, lying in the range $9.0 \times 10^6 \text{ cm}^{-2} \text{ s}^{-1} \text{ sr}^{-1} \text{ MeV}^{-1}$ – $56 \text{ cm}^{-2} \text{ s}^{-1} \text{ sr}^{-1} \text{ MeV}^{-1}$, and is a factor of 1.1–1.7 larger than the corresponding 1 in 10 year event.
2. The 1 in 10 year flux at $L = 6.5$, on field lines which map to the vicinity of geostationary orbit, decrease with increasing energy ranging from $6.2 \times 10^5 \text{ cm}^{-2} \text{ s}^{-1} \text{ sr}^{-1} \text{ MeV}^{-1}$ at $E = 0.6 \text{ MeV}$ to $0.48 \text{ cm}^{-2} \text{ s}^{-1} \text{ sr}^{-1} \text{ MeV}^{-1}$ at $E = 8.0 \text{ MeV}$. The 1 in 100 year event (red line) exhibits a similar trend, lying in the range $6.9 \times 10^5 \text{ cm}^{-2} \text{ s}^{-1} \text{ sr}^{-1} \text{ MeV}^{-1}$ – $6.0 \text{ cm}^{-2} \text{ s}^{-1} \text{ sr}^{-1} \text{ MeV}^{-1}$, and is a factor of 1.1–13 times larger than the corresponding 1 in 10 year event.
3. Our analysis suggests that the fluxes of relativistic electrons with energies in the range $0.6 < E < 2.0 \text{ MeV}$ in the region $4.25 < L < 4.75$ have an upper bound. In contrast, further out, in the region $5.5 \leq L \leq 7.0$, and at higher energies the fluxes of relativistic electrons are largely unbounded.

The 1 in N year electron fluxes determined here as a function of energy and L can serve as benchmarks against which to compare other extreme space weather events and to help assess the potential impact of an extreme event.

Data Availability Statement

The data used in this study is publicly available from <http://www.ngdc.noaa.gov/stp/space-weather/satellite-data/satellite-systems/gps/data/ns41>. The solar wind data, geomagnetic activity indices and sunspot numbers are available from the NASA GSFC OMNI website (<https://omniweb.gsfc.nasa.gov/>). The results and data shown in this study can be downloaded from the UK Polar Data Centre (<https://doi.org/10.5285/30bba6e1-de1e-4ef9-97a6-d64e9eaca820>).

Acknowledgments

We would like to acknowledge the skill and attention to detail of Timothy J. Wehner that enabled these measurements at Medium Earth Orbit. We acknowledge Los Alamos National Laboratory for generating the BDD-IIR data products used in this study, and the National Oceanic and Atmospheric Administration's archive of the data files themselves. The research leading to these results has received funding from the Natural Environment Research Council Grants NE/V00249X/1 (Sat-Risk) and NE/R016038/1.

References

- Baker, D. N., Blake, J. B., Callis, L. B., Cummings, J. R., Hovestadt, D., Kanekal, S., et al. (1994). Relativistic electron acceleration and decay time scales in the inner and outer radiation belts: SAMPEX. *Geophysical Research Letters*, 21(6), 409–412. <https://doi.org/10.1029/93GL03532>
- Baker, D. N., Kanekal, S. G., Horne, R. B., Meredith, N. P., & Glauert, S. A. (2007). Low-altitude measurements of 2–6 MeV electron trapping lifetimes at $1.5 \leq L \leq 2.5$. *Geophysical Research Letters*, 34(20), L20110. <https://doi.org/10.1029/2007GL031007>
- Baker, D. N., Kanekal, S. G., Li, X., Monk, S. P., Goldstein, J., & Burch, J. L. (2004). An extreme distortion of the Van Allen belt arising from the “Hallowe’en” solar storm in 2003. *Nature*, 432(7019), 878–881. <https://doi.org/10.1038/nature03116>
- Blake, J. B., Kolasinski, W. A., Fillius, R. W., & Mullen, E. G. (1992). Injection of electrons and protons with energies of tens of MeV into $L < 3$ on 24 March 1991. *Geophysical Research Letters*, 19(8), 821–824. <https://doi.org/10.1029/92GL00624>
- Cayton, T. E., Belian, R. D., Gary, S. P., Fritz, T. A., & Baker, D. N. (1989). Energetic electron components at geosynchronous orbit. *Geophysical Research Letters*, 16(2), 147–150. <https://doi.org/10.1029/GL016i002p00147>
- Cayton, T. E., Chen, Y., Friedel, R. H. W., & Kippen, R. M. (2010). *Analysis of electron and proton environmental data for medium Earth orbit (2000–present)*. Technical Report LA-UR-10-04234. Los Alamos National Laboratory.
- Cayton, T. E., Drake, D. M., Spencer, K. M., Herrin, M., Wehner, T. J., & Reedy, R. C. (1998). *Description of the BDD-IIR: Electron and proton sensors on the GPS*. Technical Report LA-UR-98-1162. Los Alamos National Laboratory.
- Coles, S. (2001). *An introduction to statistical modelling of extreme values*. Springer.
- Della-Marta, P. M., Mathis, H., Frei, C., Liniger, M. A., Kleinn, J., & Appenzeller, C. (2009). The return period of wind storms over Europe. *International Journal of Climatology*, 29(3), 437–459. <https://doi.org/10.1002/joc.1794>
- Denton, M. H., & Cayton, T. E. (2011). Density and temperature of energetic electrons in the Earth's magnetotail derived from high-latitude GPS observations during the declining phase of the solar cycle. *Annales Geophysicae*, 29(10), 1755–1763. <https://doi.org/10.5194/angeo-29-1755-2011>
- Dey, A. K., & Das, K. P. (2016). Modeling extreme hurricane damage using the generalized Pareto distribution. *American Journal of Mathematical and Management Sciences*, 35(1), 55–66. <https://doi.org/10.1080/01966324.2015.1075926>
- Elvidge, S., & Angling, M. J. (2018). Using extreme value theory for determining the probability of Carrington-like solar flares. *Space Weather*, 16(4), 417–421. <https://doi.org/10.1002/2017SW001727>
- EUSPA EO and GNSS Market Report. (2022). Retrieved from https://www.euspa.europa.eu/sites/default/files/uploads/euspa_market_report_2022.pdf

- Frederickson, A. R., Mullen, E. G., Brautigam, D. H., Kerns, K. J., & Holman, E. G. (1991). Radiation induced insulator discharge pulses in the CRRES internal discharge monitor satellite experiment. *IEEE Transactions on Nuclear Science*, 38(6), 778–784. <https://doi.org/10.1109/23.124153>
- Hapgood, M., Angling, M. J., Attrill, G., Bisi, M., Cannon, P. S., Dyer, C., et al. (2021). Development of space weather reasonable worst-case scenarios for the UK National Risk Assessment. *Space Weather*, 19. <https://doi.org/10.1029/2020SW002593>
- HM Government, National Risk Register. (2020). Retrieved from <https://www.gov.uk/government/publications/national-risk-register-2020>
- Horne, R. B., Phillips, M. W., Glauert, S. A., Meredith, N. P., Hands, A. D. P., Ryden, K., & Li, W. (2018). Realistic worst case for a severe space weather event driven by a fast solar wind stream. *Space Weather*, 16(9), 1202–1215. <https://doi.org/10.1029/2018SW001948>
- Horne, R. B., Thorne, R. M., Shprits, Y. Y., Meredith, N. P., Glauert, S. A., Smith, A. J., et al. (2005). Wave acceleration of electrons in the Van Allen radiation belts. *Nature*, 437(7056), 227–230. <https://doi.org/10.1038/nature03939>
- Iucci, N., Levitin, A. E., Belov, A. V., Eroshenko, E. A., Ptitsyna, N. G., Villoresi, G., et al. (2005). Space weather conditions and spacecraft anomalies in different orbits. *Space Weather*, 3(1), S01001. <https://doi.org/10.1029/2003SW000056>
- Johnston, W. R., O'Brien, T. P., Ginet, G. P., Huston, S. L., Guild, T. B., & Fennelly, J. A. (2014). AE9/AP9/SPM: New models for radiation belt and space plasma specification. *Proceedings of SPIE*, 9085.
- Koller, J., Chen, Y., Reeves, G. D., Friedel, R. H. W., Cayton, T. E., & Vrugt, J. A. (2007). Identifying the radiation belt source region by data assimilation. *Journal of Geophysical Research*, 112(A6), A06244. <https://doi.org/10.1029/2006JA012196>
- Koons, H. C., & Fennel, J. F. (2006). Space weather effects on communications satellites. *URSI Radio Science Bulletin*, 316, 27–41.
- Krausmann, E. (2011). The space-weather awareness dialogue: Findings and outlook. JRC Scientific and Technical Reports (pp. 25–26).
- Li, W., & Hudson, M. K. (2019). Earth's Van Allen radiation belts: From discovery to the Van Allen Probes era. *Journal of Geophysical Research: Space Physics*, 124(11), 8319–8351. <https://doi.org/10.1029/2018JA025940>
- Li, Y., Cai, W., & Campbell, E. P. (2005). Statistical modeling of extreme rainfall in southwest western Australia. *Journal of Climate*, 18(6), 852–863. <https://doi.org/10.1175/JCLI-3296.1>
- Meredith, N. P., Cain, M., Horne, R. B., Thorne, R. M., Summers, D., & Anderson, R. R. (2003). Evidence for chorus-driven electron acceleration to relativistic energies from a survey of geomagnetically disturbed periods. *Journal of Geophysical Research*, 108(A6), 1248. <https://doi.org/10.1029/2002JA009764>
- Meredith, N. P., Horne, R. B., Isles, J. D., & Green, J. C. (2016a). Extreme energetic electron fluxes in low Earth orbit: Analysis of POES $E > 30$, $E > 100$ and $E > 300$ keV electrons. *Space Weather*, 14(2), 136–150. <https://doi.org/10.1002/2015SW001348>
- Meredith, N. P., Horne, R. B., Isles, J. D., & Rodriguez, J. V. (2015). Extreme relativistic electron fluxes at geosynchronous orbit: Analysis of GOES $E > 2$ MeV electrons. *Space Weather*, 13(3), 170–184. <https://doi.org/10.1002/2014SW001143>
- Meredith, N. P., Horne, R. B., Isles, J. D., Ryden, K. A., Hands, A. D. P., & Heynderickx, D. (2016b). Extreme internal charging currents in medium Earth orbit: Analysis of SURF plate currents on Giove-A. *Space Weather*, 14(8), 57–591. <https://doi.org/10.1002/2016SW001404>
- Meredith, N. P., Horne, R. B., Sandberg, I., Papadimitriou, C., & Evans, H. D. R. (2017). Extreme relativistic electron fluxes in the Earth's outer radiation belt: Analysis of INTEGRAL IREM data. *Space Weather*, 15(7), 917–933. <https://doi.org/10.1002/2017SW001651>
- Messenger, S. R., Jackson, E. M., Warner, J. H., Walters, R. J., Cayton, T. E., Chen, Y., et al. (2011). Correlation of telemetered solar array data with particle detector data on GPS spacecraft. *IEEE Transactions on Nuclear Science*, 58(6), 3118–3125. <https://doi.org/10.1109/TNS.2011.2172957>
- Nogaj, M., Yiou, P., Parey, S., Malek, F., & Naveau, P. (2006). Amplitude and frequency of temperature extremes over the North Atlantic region. *Geophysical Research Letters*, 33(10), L10801. <https://doi.org/10.1029/2005GL024251>
- O'Brien, T. P., Johnston, W. R., Huston, S. L., Roth, C. J., Guild, T. B., Su, Y.-J., & Quinn, R. A. (2018). Changes in AE8/AP9-IRENE version 1.5. *IEEE Transactions on Nuclear Science*, 65(1), 462–466. <https://doi.org/10.1109/TNS.2017.2771324>
- Olson, W. P., & Pfizter, K. (1977). *Magnetospheric magnetic field modelling annual scientific report*. Air Force Office of Scientific Research.
- Picklands, J. (1975). Statistical inference using extreme order statistics. *Annals of Statistics*, 3, 119–131.
- Pierrard, V., & Lemaire, J. (1996). Fitting AE8 energy spectra with two Maxwellian functions. *Radiation Measurements*, 26(3), 333–337. [https://doi.org/10.1016/1350-4487\(96\)00057-1](https://doi.org/10.1016/1350-4487(96)00057-1)
- R Development Core Team. (2008). *R: A language and environment for statistical computing*. R Foundation for Statistical Computing. ISBN 3-900051-07-0 Retrieved from <http://www.R-project.org>
- Reagan, J. B., Nightingale, R. W., Gaines, E. E., Imhof, W. L., & Stassinopoulos, E. G. (1981). Outer zone energetic electron spectral measurements. *Journal of Spacecraft and Rockets*, 18(1), 83–88. <https://doi.org/10.2514/3.57791>
- Reeves, G. D., Chen, Y., Cunningham, G. S., Friedel, R. W. H., Henderson, M. G., Jordanova, V. K., et al. (2012). Dynamic radiation environment assimilation model: DREAM. *Space Weather*, 10(3), S03006. <https://doi.org/10.1029/2011SW000729>
- Rodgers, D. J., & Ryden, K. A. (2001). Internal charging in space. In R. A. Harris & (Eds.), *Proceedings of 7th spacecraft charging technology conference, Noordwijk, The Netherlands, 23–27 April, ESA SP-476* (p. 25). European Space Agency.
- Satellite Industry Association. (2022). State of the satellite industry report 2022. Retrieved from <https://sia.org/news-resources/state-of-the-satellite-industry-report>
- Shprits, Y., Subbotin, D., Ni, B., Horne, R., Baker, D., & Cruce, P. (2011). Profound change of the near-Earth radiation environment caused by solar superstorms. *Space Weather*, 9(8), S08007. <https://doi.org/10.1029/2011SW000662>
- Shprits, Y. Y., Elkington, S. R., Meredith, N. P., & Subbotin, D. A. (2008). Review of modeling of losses and sources of relativistic electrons in the outer radiation belt I: Radial transport. *Journal of Atmospheric and Solar-Terrestrial Physics*, 70(14), 1679–1693. <https://doi.org/10.1016/j.jastp.2008.06.008>
- Shprits, Y. Y., Subbotin, D. A., Meredith, N. P., & Elkington, S. R. (2008). Review of modeling of losses and sources of relativistic electrons in the outer radiation belt II: Local acceleration and loss. *Journal of Atmospheric and Solar-Terrestrial Physics*, 70(14), 1694–1713. <https://doi.org/10.1016/j.jastp.2008.06.014>
- Tebaldi, C. B., Strauss, H., & Zervas, C. E. (2012). Modelling sea level rise impacts on storm surges along U.S. coasts. *Environmental Research Letters*, 7(1), 14032. <https://doi.org/10.1088/1748-9326/7/1/014032>
- Thomson, A. W. P., Dawson, E. B., & Reay, S. J. (2011). Quantifying extreme behavior in geomagnetic activity. *Space Weather*, 9(10), S10001. <https://doi.org/10.1029/2011SW000696>
- Thorne, R. M. (2010). Radiation belt dynamics: The importance of wave-particle interactions. *Geophysical Research Letters*, 37(22), L22107. <https://doi.org/10.1029/2010GL044990>
- Tsubouchi, K., & Omura, Y. (2007). Long-term occurrence probabilities of intense geomagnetic storm events. *Space Weather*, 5(12), S12003. <https://doi.org/10.1029/2007SW000329>
- Tuszewski, M., Cayton, T. E., & Ingraham, J. C. (2002). A new numerical technique to design satellite energetic electron detectors. *Nuclear Instruments & Methods in Physics Research, Section A*, 482(3), 653–666. [https://doi.org/10.1016/S0168-9002\(01\)01735-1](https://doi.org/10.1016/S0168-9002(01)01735-1)

- US Space Weather Benchmarks Phase 1 Report. (2018). Retrieved from <https://www.sworm.gov/publications/2018/Space-Weather-Phase-1-Benchmarks-Report.pdf>
- Varotsou, A., Friedel, R. H., Reeves, G. D., Lavraud, B., Skoug, R. M., Cayton, T. E., & Bourdarie, S. (2008). Characterization of relativistic electron flux rise times during the recovery phase of geomagnetic storms as measured by the NA41 GPS satellite. *Journal of Atmospheric and Solar-Terrestrial Physics*, 70(14), 1745–1759. <https://doi.org/10.1016/j.jastp.2008.01.020>
- Webb, F. D., & Allen, J. H. (2004). Spacecraft and ground anomalies related to the October–November 2003 solar activity. *Space Weather*, 2(3), S03008. <https://doi.org/10.1029/2004SW000075>
- Wrenn, G. L., Rodgers, D. J., & Ryden, K. A. (2002). A solar cycle of spacecraft anomalies due to internal charging. *Annales Geophysicae*, 20(7), 953–956. <https://doi.org/10.5194/angeo-20-953-2002>